Chapter 13

Fitting the HRMA Effective Area

Michael Tibbetts

13.1 Introduction

This chapter deals with the effort to improve the agreement between the XRCF effective area data and the HRMA mirror models. We consider the effective areas derived from the solid state detector (SSD) continuum data, and attempt to fit the data by allowing the surface roughness value, σ, in the model to vary. Since σ is energy independent, we would expect to fit the effective area with a single value of σ for each optic. However, with the SSD continuum data, it is only possible to isolate each shell, a hyperboloid-paraboloid pair. The fits are further complicated by the fact that the optical constants for each optic were determined from a single witness coupon from the p6 optic, coupon 065. The optical constants for this coupon were determined by fitting reflectivity data taken by the MST synchrotron group. Due to limitations on the range of the energy scale available with a given setup at the synchrotron, the reflectivity data were taken over multiple energy ranges. Each energy range was fit independently by varying the value of σ in the model of the witness coupon. Thus, the SSD continuum simulations contain optical constants derived from measurements of a single optic but applied to all optics. Also, the optical constants from the synchrotron reflectivity data allow the value of σ to vary between energy ranges.

In fitting the SSD continuum data, we begin by fitting the effective area with a single value of σ applied over the entire energy range. It will be shown that the effective areas derived in this manner fit the data poorly. From there we fit the data over multiple energy ranges corresponding to the energy ranges used in deriving the optical constants from the synchrotron data. These fits show varied results based on energy range and shell.

13.2 Mirror Model

The simulations treat the mirrors as multi-layered surfaces comprised of a layer of Iridium, a layer of Chromium, and a layer of Zerodur in a vacuum, as illustrated in figure 13.1.

At the interface of each layer, including the vacuum-Iridium interface, the simulations calculate the reflection and transmission coefficients. The reflection coefficient, r_t, for the top interface can be calculated recursively using the following formula:

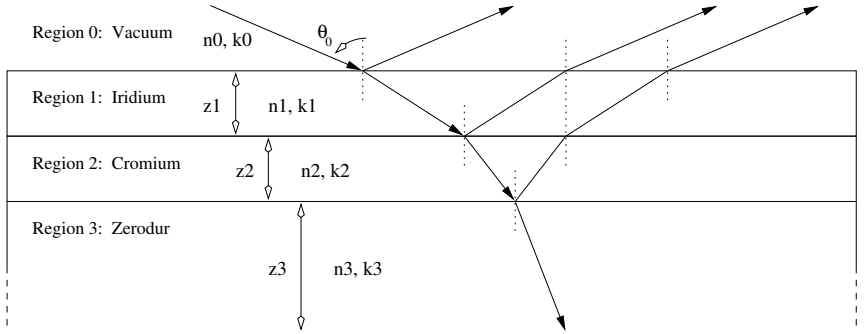

Figure 13.1: Reflection and transmission through a multi-layer mirror.

$$r_t = r_{ij} + \frac{r_b t_{ij} t_{ji} e^{2i\beta_j}}{1 + r_{ij} r_b e^{2i\beta_j}} \tag{13.1}$$

where r_{ij} is the reflection coefficient for the interface between the i-th and j-th layers, r_b is the reflection coefficient from the bottom layer, t_{ij} and t_{ji} are the transmission coefficients into and out of the interface, and β_j is defined below.

$$\beta_j = \frac{2\pi n_j z_j \cos\theta_j}{\lambda} \tag{13.2}$$

where n_j is the optical constant from layer j, z_j is the layer thickness, θ_j is the incidence angle, and λ is the wavelength. The reflection coefficients above are obtained from a modified version of the Fresnel equations:

$$r^s_{ij} = \frac{n_i \cos\theta_i - n_j \cos\theta_j}{n_i \cos\theta_i + n_j \cos\theta_j} \exp^{-2[\frac{2\pi\sigma_{ij}\cos\theta_i}{\lambda}]^2} \tag{13.3}$$

$$r^p_{ij} = \frac{n_i \cos\theta_j - n_j \cos\theta_i}{n_i \cos\theta_j + n_j \cos\theta_i} \exp^{-2[\frac{2\pi\sigma_{ij}\cos\theta_i}{\lambda}]^2} \tag{13.4}$$

where $\exp^{-2[\frac{2\pi\sigma_{ij}\cos\theta_i}{\lambda}]^2}$ is the Debye-Waller factor at the interface between layers i and j accounting for the reflection lose due to scattering. It is in this modifying factor that the surface roughness term, σ, is applied. From equations 13.3 and 13.4, we see that a different value of σ can be applied for each surface interface.

We know that the optical constants derived from the synchrotron measurements fit the value of σ for each interface separately. However, it was determined that the value of σ used for the vacuum Iridium interface was the dominant factor and so we simplify and use the same value of σ at each interface.

13.3 Setup

The simulations represent measurements with a 2mm aperture located on-axis at the focal plane. The rays use the `xrcf_xss_03` configuration of `trace-xrcf1`. Complete descriptions of the software and this configuration can be found at:

`http://hea-www.harvard.edu/MST/simul/raytrace/databases/ts_config/00Index.html`. Each simulated effective area has a statistical error $\leq 1\%$, corresponding to poisson statistics for the number of photons in the simulation. In order to get a feel for systematic variations in the simulations, due to the probabilistic nature of the reflectivity in the simulations, we ran 10 distinct simulations of each data set. Each simulation was started with a different seed for the random number generator in the simulation. This allows us to gain an understanding of any systematic variations in the experiment.

13.4 Fitting

We began by fitting the SSD continuum data over the range of 2 to 10.5 KeV with a single value of σ for the entire energy range. Since the value of σ should be independent of energy, we would expect a single value to provide a good fit. Figures 13.2to13.5 show the results of the 10 simulated data sets to the SSD data over the entire energy range for shells 1, 3, 4, and 6. Table 13.1 shows the resulting reduced χ^2 of the fits. The reduced χ^2 of the fits indicate that a single value of σ over the entire energy range fits the data poorly.

From there, we broke up the SSD continuum data and fit each energy range used to determine the optical constants independently. The energy ranges are 2.01 to 2.4 KeV, 2.25 to 2.9 KeV, 2.8 to 4 KeV, 3.9 to 7 KeV, 5 to 8.5 KeV, 8 to 12 KeV. For each energy range, except 2.01 to 2.4 KeV, we took 5 or 6 evenly distributed data points from the SSD continuum data to constitute the data set to be fit. For the 2.01 to 2.4 KeV range, we were only able to get two points at the higher end of the range. Results of the fits are in Figures 13.6to13.29.

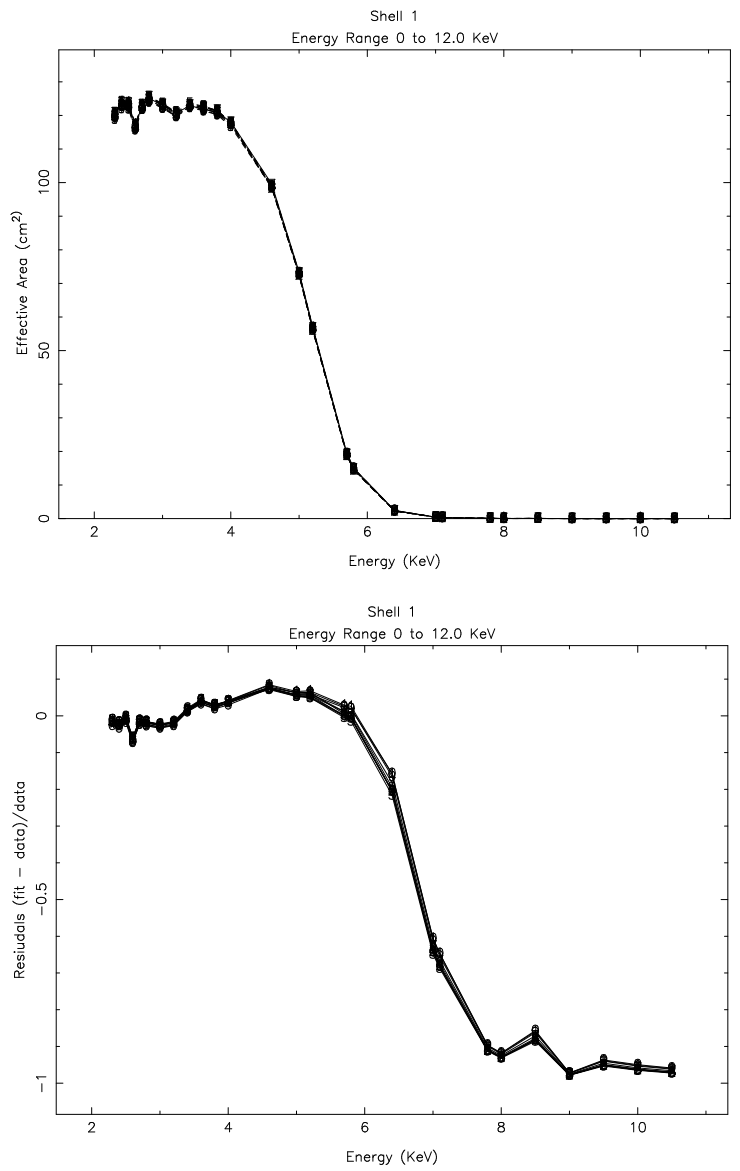

Figure 13.2: SSD continuum data and model effective area and residuals through 2mm pinhole for shell 1.

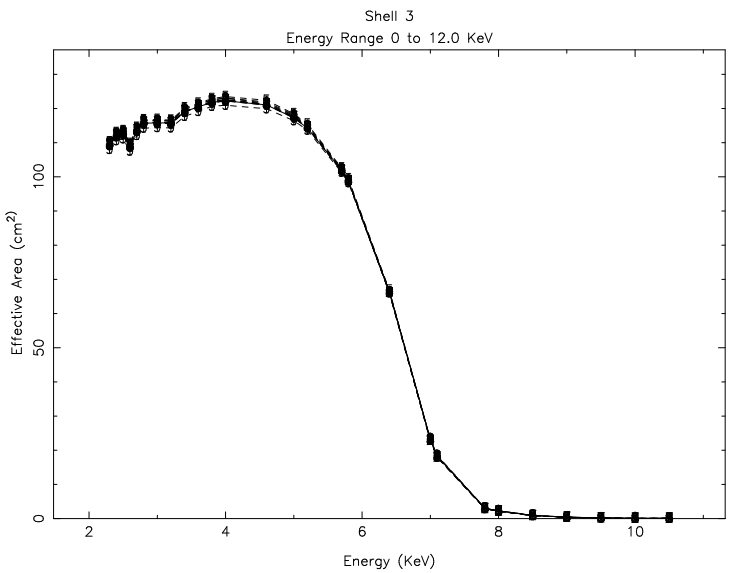

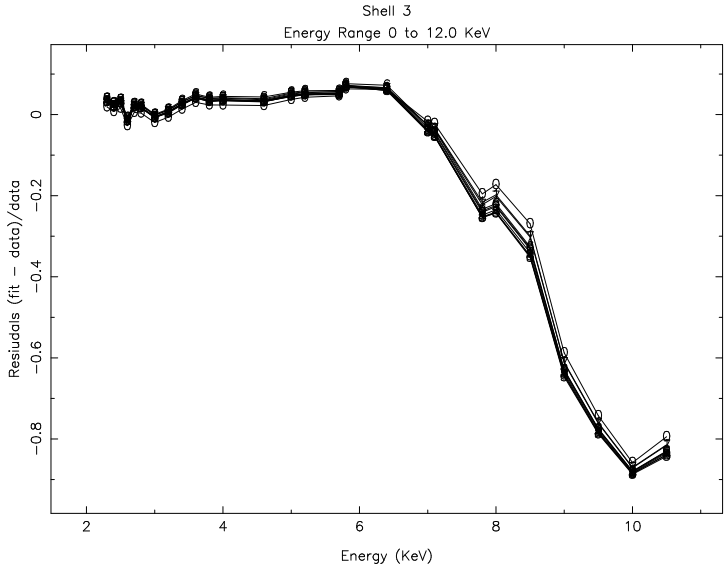

Figure 13.3: SSD continuum data and model effective area and residuals through 2mm pinhole for shell 3.

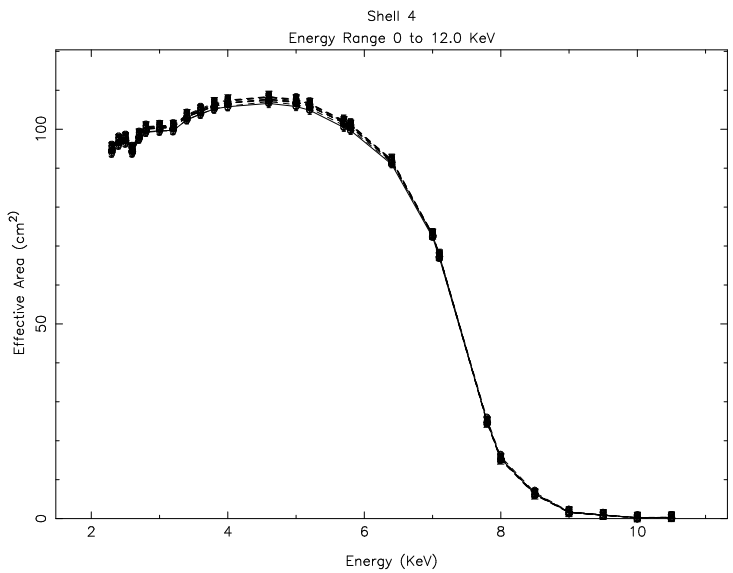

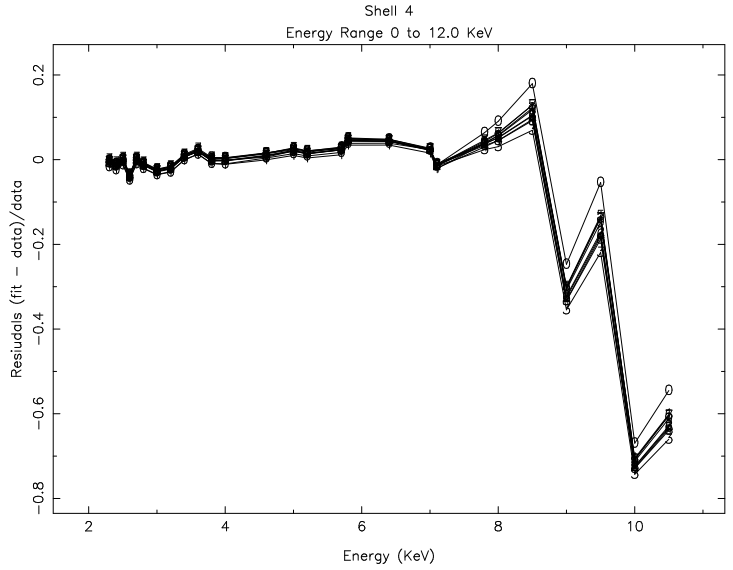

Figure 13.4: SSD continuum data and model effective area and residuals through 2mm pinhole for shell 4.

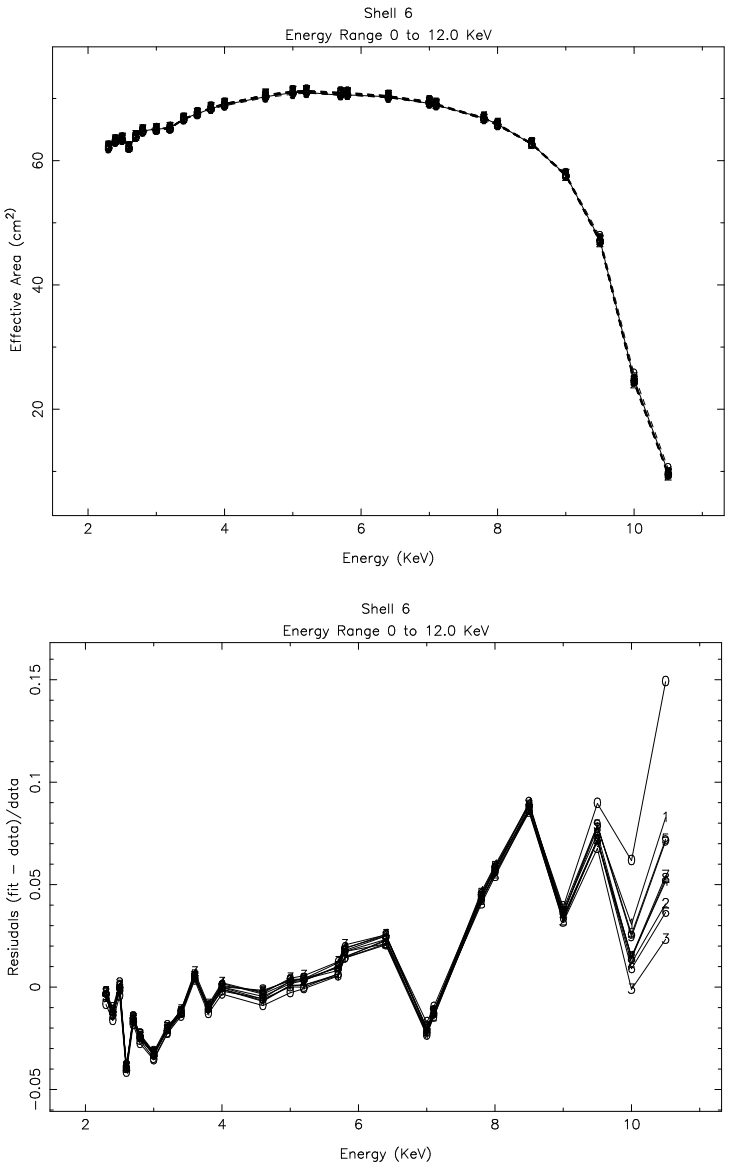

Figure 13.5: SSD continuum data and model effective area and residuals through 2mm pinhole for shell 6.

Shell	Energy	Seed	Reduced χ^2	$\sigma_{\rm Aeff}$
1	0.00 12.00	1	19.2330	7.6656
1	0.00 12.00	2	19.7227	8.1168
1	0.00 12.00	3	19.9562	8.1910
1	0.00 12.00	4	19.9521	8.0996
1	0.00 12.00	5	19.8950	8.1240
1	0.00 12.00	6	19.6568	8.1425
1	0.00 12.00	7	19.6705	7.9039
1	0.00 12.00	8	19.7442	8.0414
1	0.00 12.00	9	19.2286	7.7272
1	0.00 12.00	10	19.2790	7.5835
3	0.00 12.00	1	13.3453	4.0237
3	0.00 12.00	2	15.3185	4.5000
3	0.00 12.00	3	15.8722	4.8129
3	0.00 12.00	4	14.9886	4.7114
3	0.00 12.00	5	14.4998	4.6099
3	0.00 12.00	6	15.8168	4.5000
3	0.00 12.00	7	13.3185	4.0564
3	0.00 12.00	8	14.9630	4.7026
3	0.00 12.00	9	14.4518	4.5000
3	0.00 12.00	10	11.3052	3.4314
4	0.00 12.00	1	5.0807	3.7612
4	0.00 12.00	2	5.2083	4.4369
4	0.00 12.00	3	5.4712	4.9685
4	0.00 12.00	4	5.1740	4.5000
4	0.00 12.00	5	5.0365	3.9478
4	0.00 12.00	6	5.3174	4.5000
4	0.00 12.00	7	5.0377	3.9362
4	0.00 12.00	8	5.2685	4.6244
4	0.00 12.00	9	5.0129	4.0726
4	0.00 12.00	10	5.4154	2.5079
6	0.00 12.00	1	2.6173	4.9975
6	0.00 12.00	2	2.3277	6.1460
6	0.00 12.00	3	2.4088	6.5383
6	0.00 12.00	4	2.6018	5.9270
6	0.00 12.00	5	2.6323	5.3034
6	0.00 12.00	6	2.4617	6.2584
6	0.00 12.00	7	2.4635	5.6968
6	0.00 12.00	8	2.4132	5.9473
6	0.00 12.00	9	2.6884	5.4510
6	0.00 12.00	10	3.1549	2.5405

Table 13.1: Shells 1, 3, 4, and 6 reduced χ^2 and σ

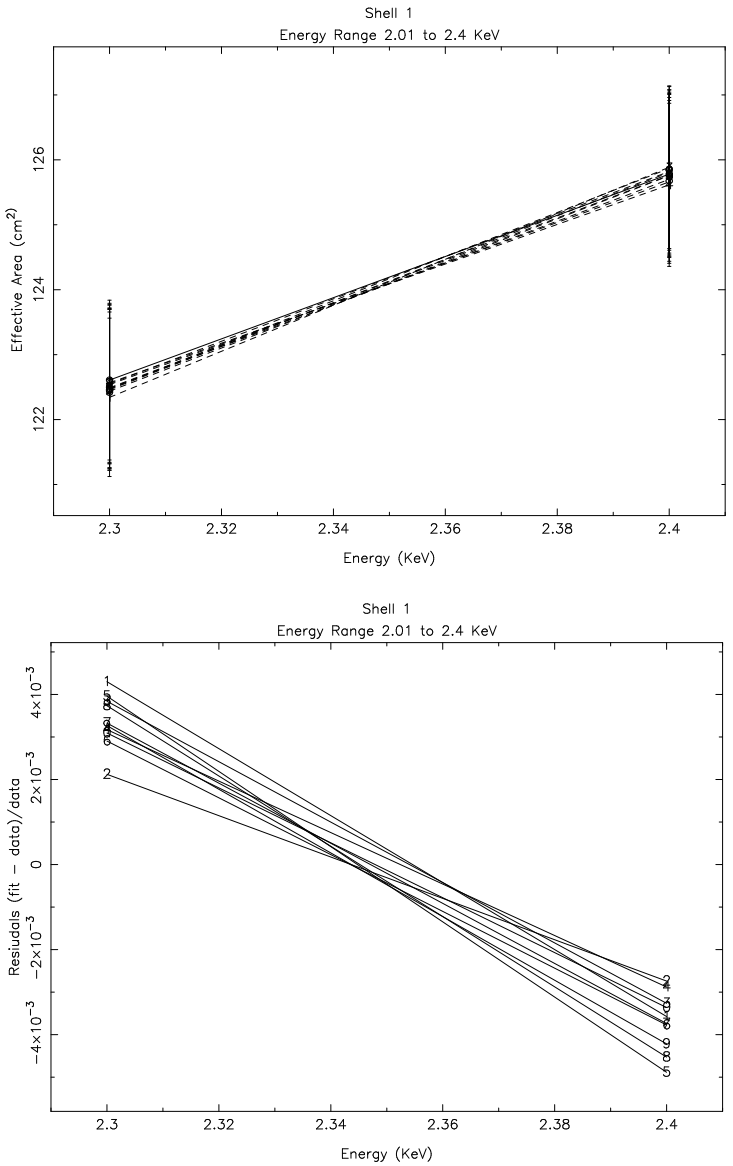

Figure 13.6: SSD continuum data and model effective area and residuals through 2mm pinhole for shell 1 between 2.01 and 2.4 keV.

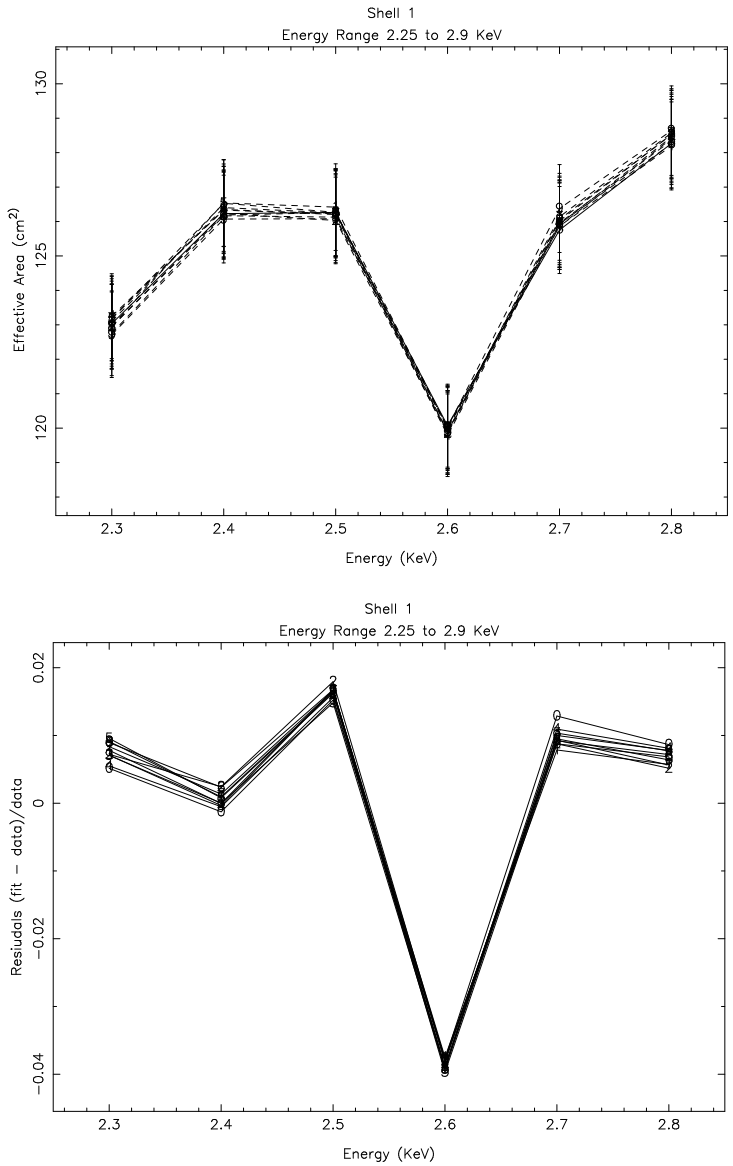

Figure 13.7: SSD continuum data and model effective area and residuals through 2mm pinhole for shell 1 between 2.25 and 2.9 keV.

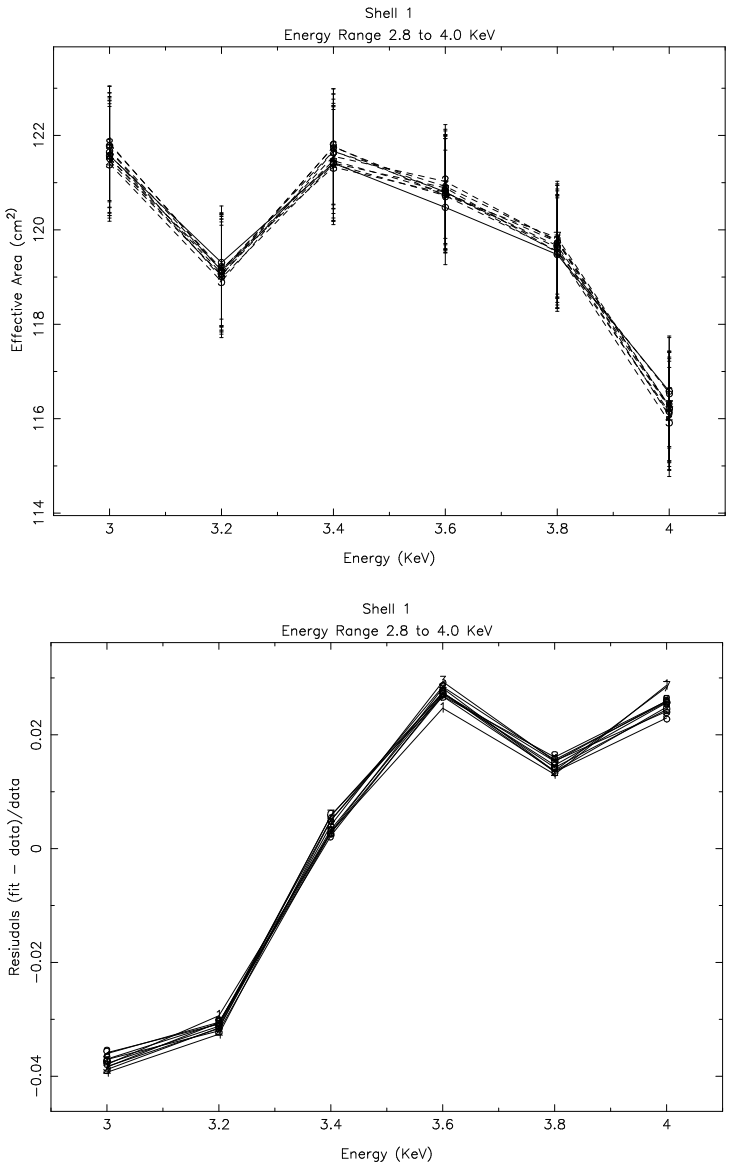

Figure 13.8: SSD continuum data and model effective area and residuals through 2mm pinhole for shell 1 between 2.8 and 4.0 keV.

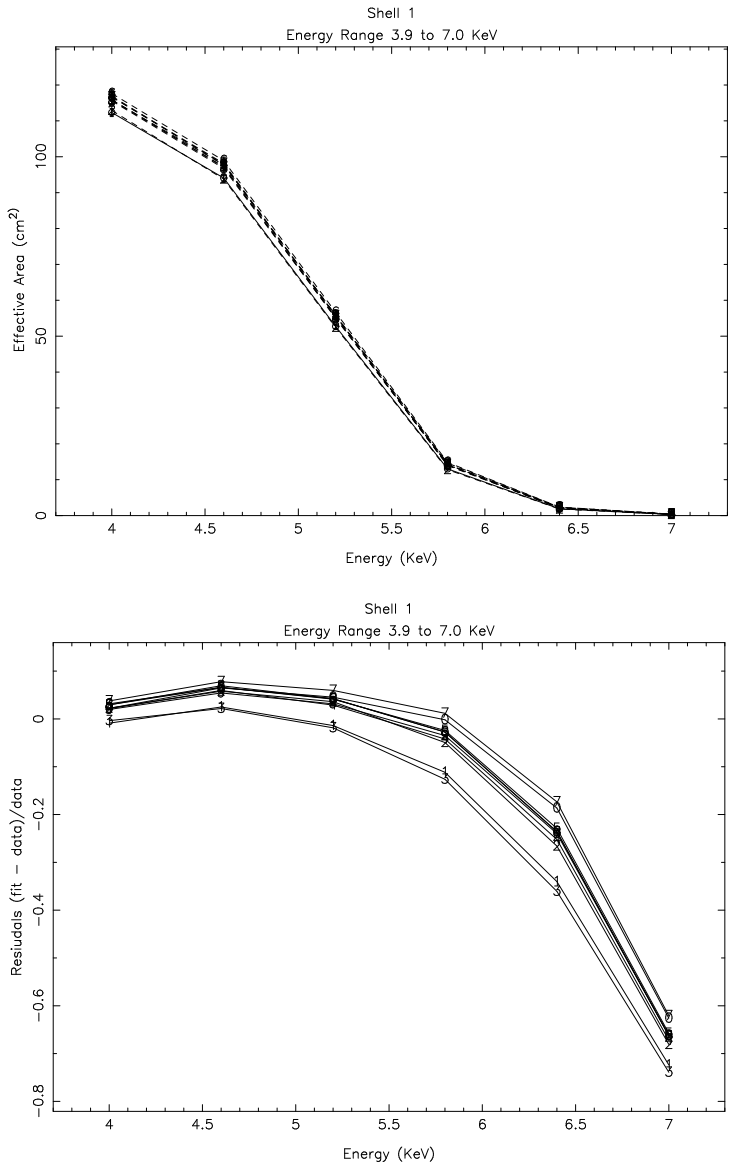

Figure 13.9: SSD continuum data and model effective area and residuals through 2mm pinhole for shell 1 between 3.9 and 7.0 keV.

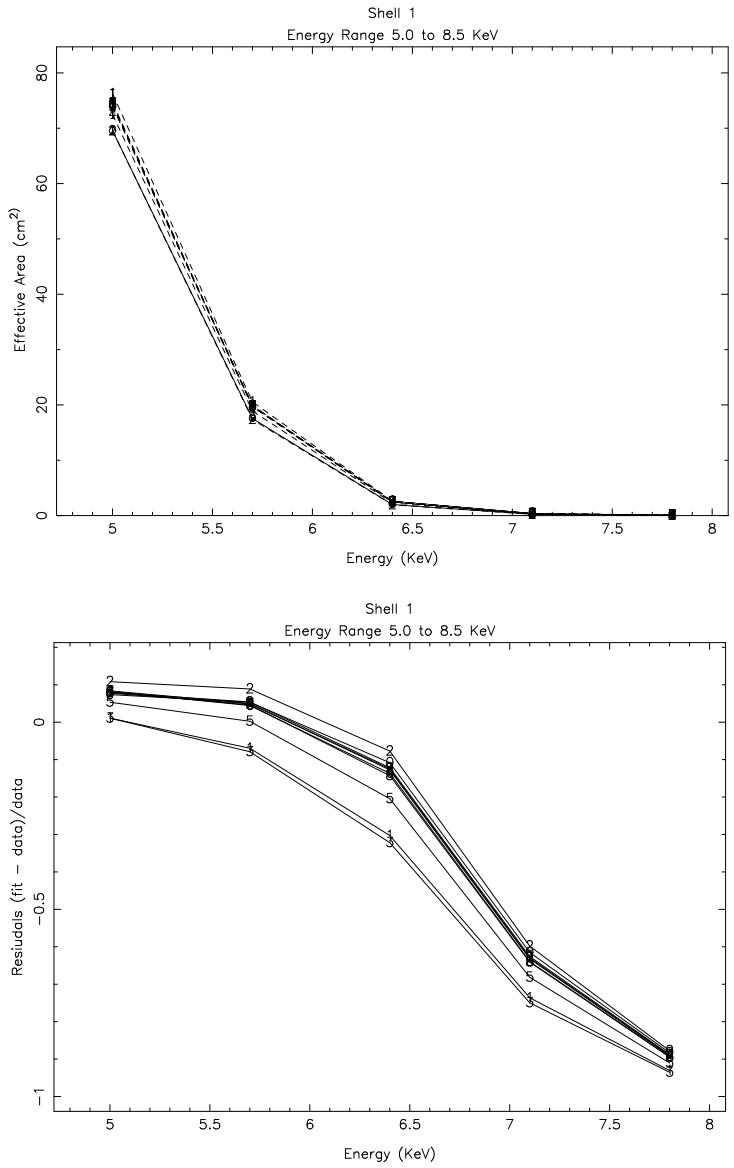

Figure 13.10: SSD continuum data and model effective area and residuals through 2mm pinhole for shell 1 between 5.0 and 8.5 keV.

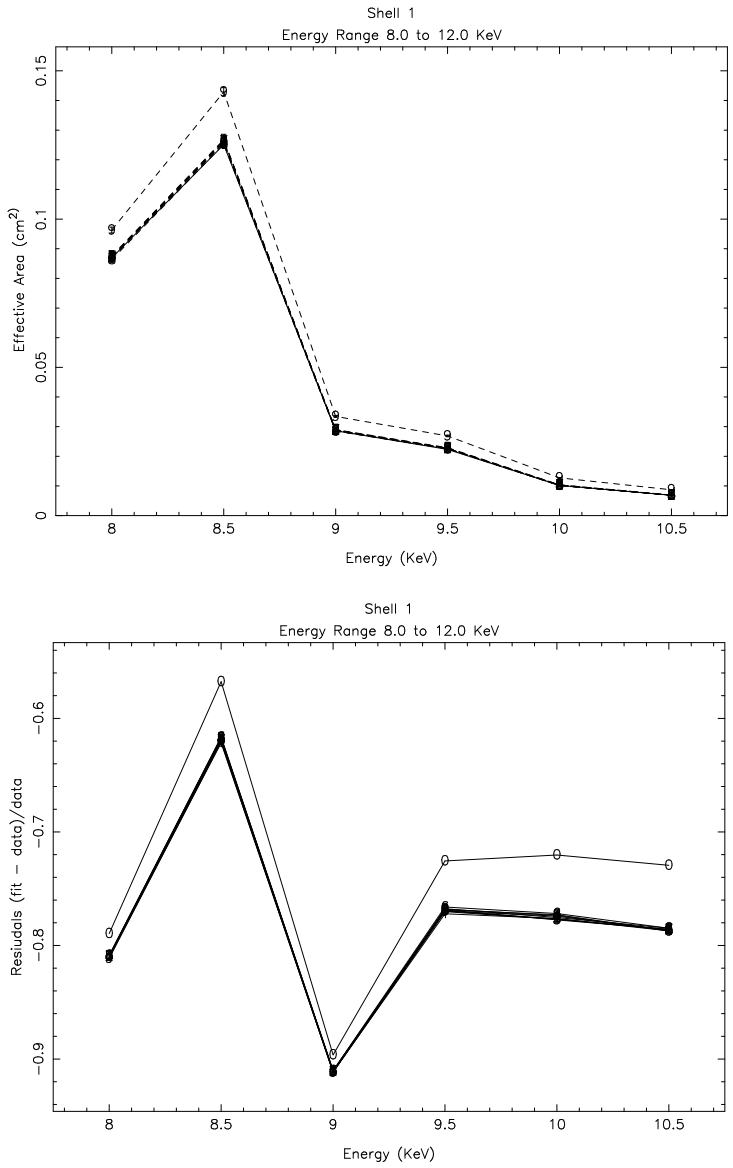

Figure 13.11: SSD continuum data and model effective area and residuals through 2mm pinhole for shell 1 between 8.0 and 12.0 keV.

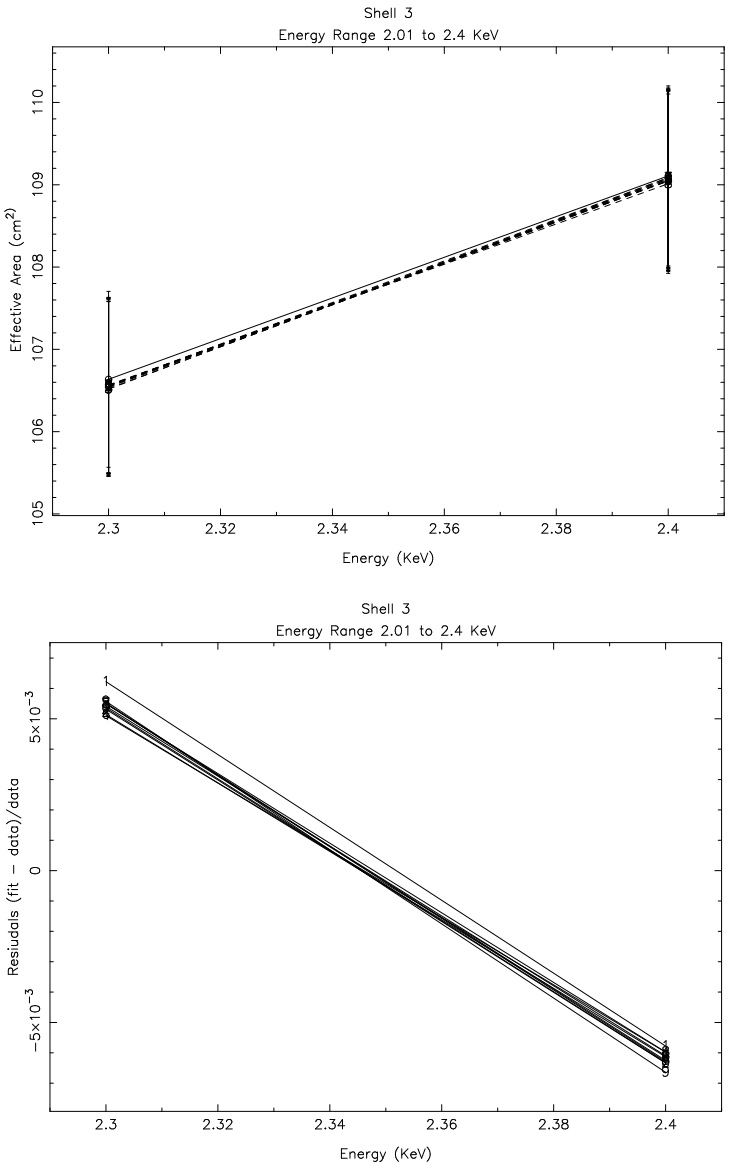

Figure 13.12: SSD continuum data and model effective area and residuals through 2mm pinhole for shell 3 between 2.01 and 2.4 keV.

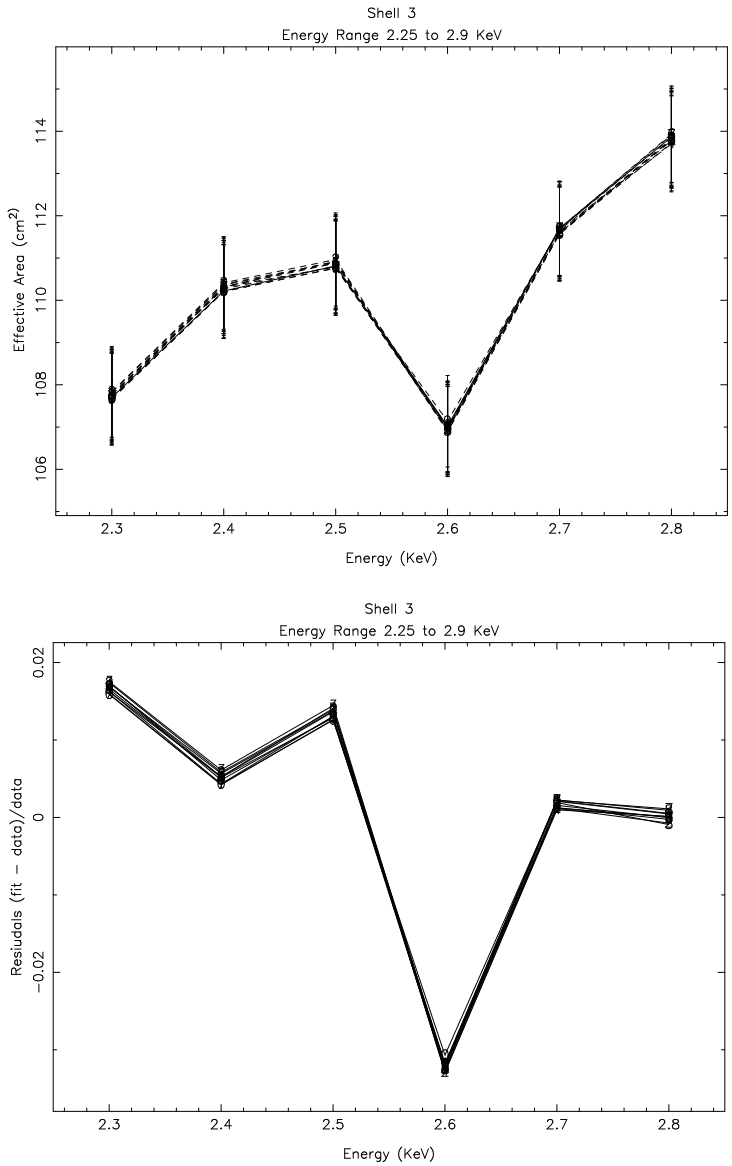

Figure 13.13: SSD continuum data and model effective area and residuals through 2mm pinhole for shell 3 between 2.25 and 2.9 keV.

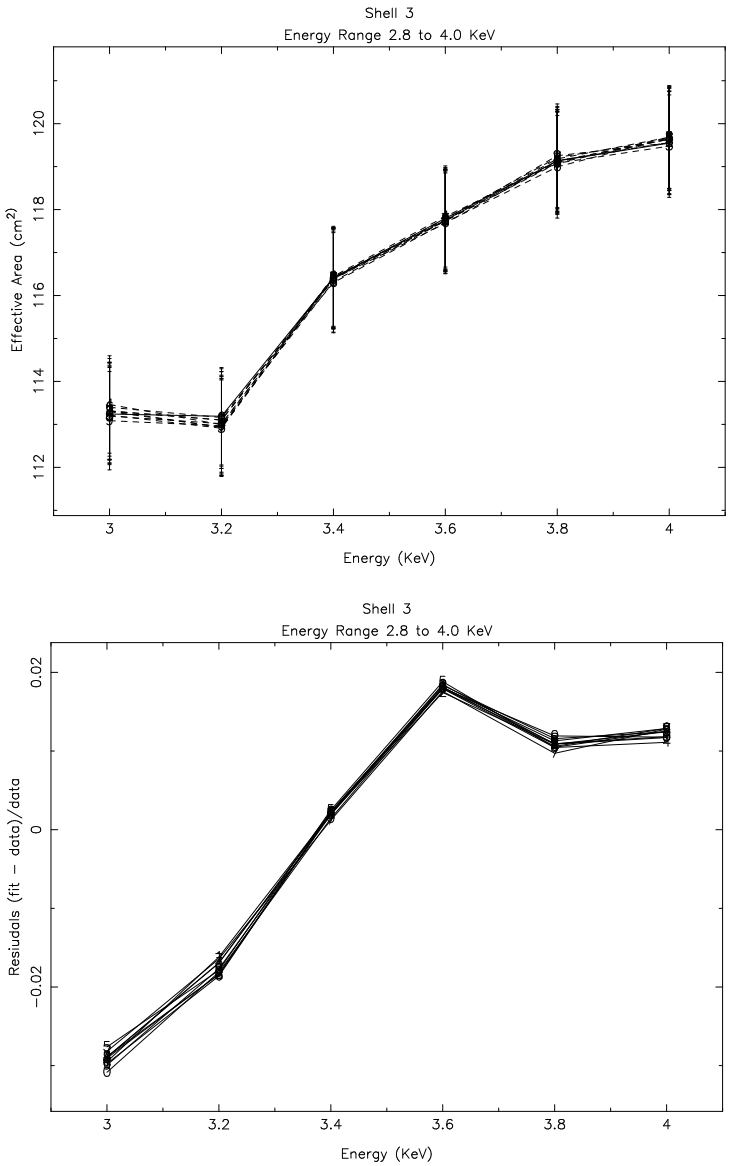

Figure 13.14: SSD continuum data and model effective area and residuals through 2mm pinhole for shell 3 between 2.8 and 4.0 keV.

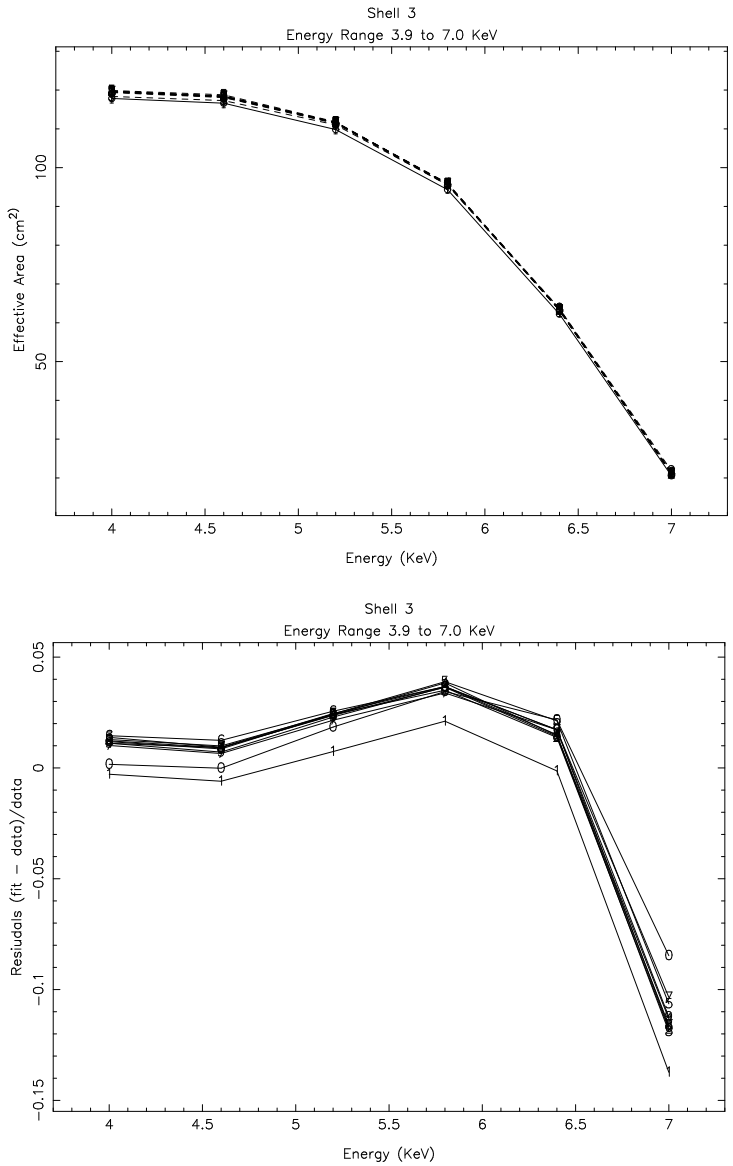

Figure 13.15: SSD continuum data and model effective area and residuals through 2mm pinhole for shell 3 between 3.9 and 7.0 keV.

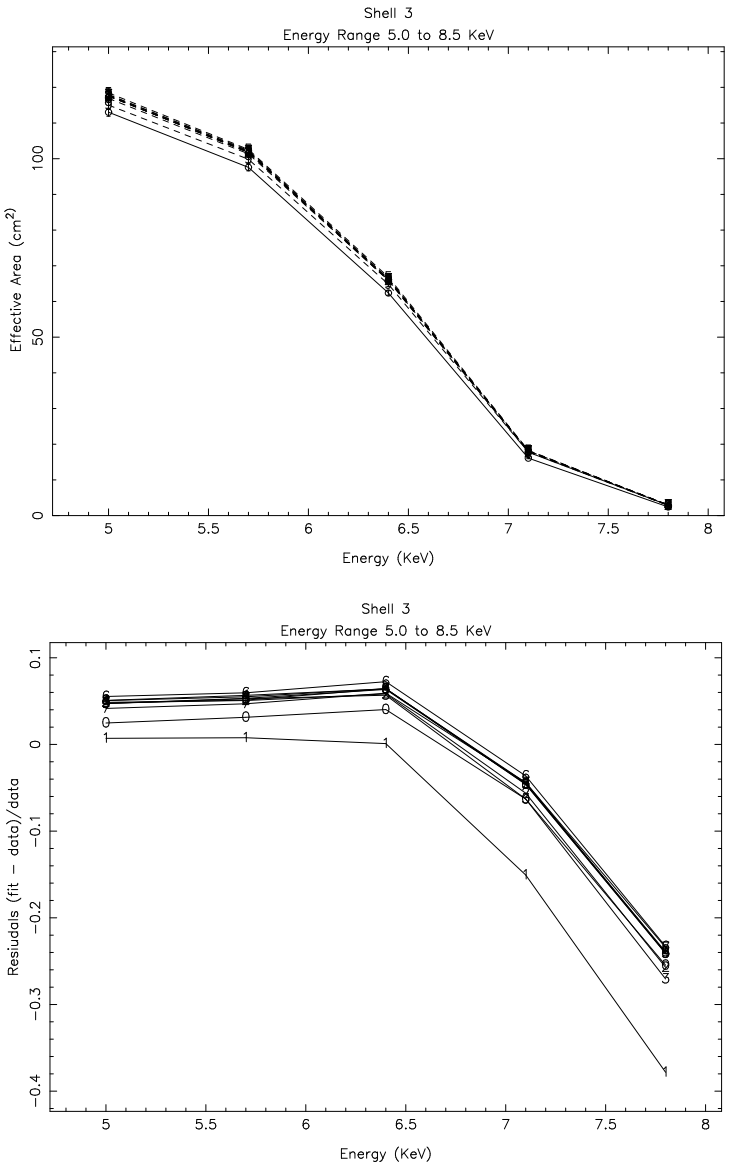

Figure 13.16: SSD continuum data and model effective area and residuals through 2mm pinhole for shell 3 between 5.0 and 8.5 keV.

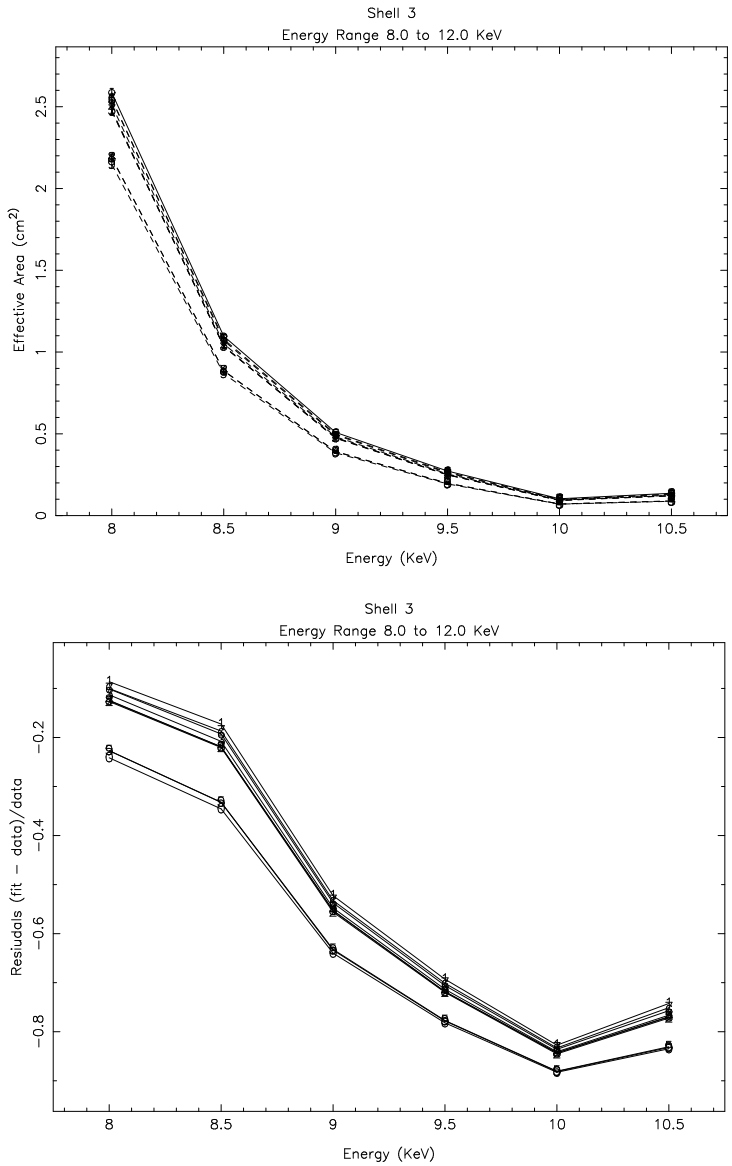

Figure 13.17: SSD continuum data and model effective area and residuals through 2mm pinhole for shell 3 between 8.0 and 12.0 keV.

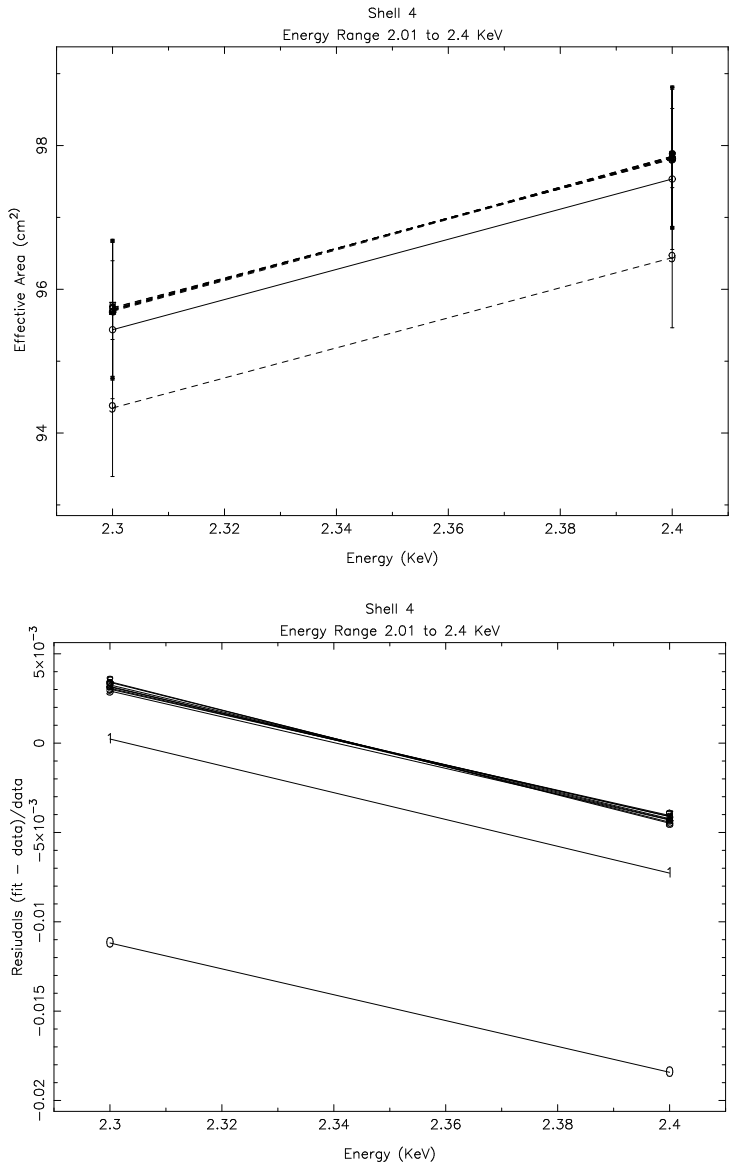

Figure 13.18: SSD continuum data and model effective area and residuals through 2mm pinhole for shell 4 between 2.01 and 2.4 keV.

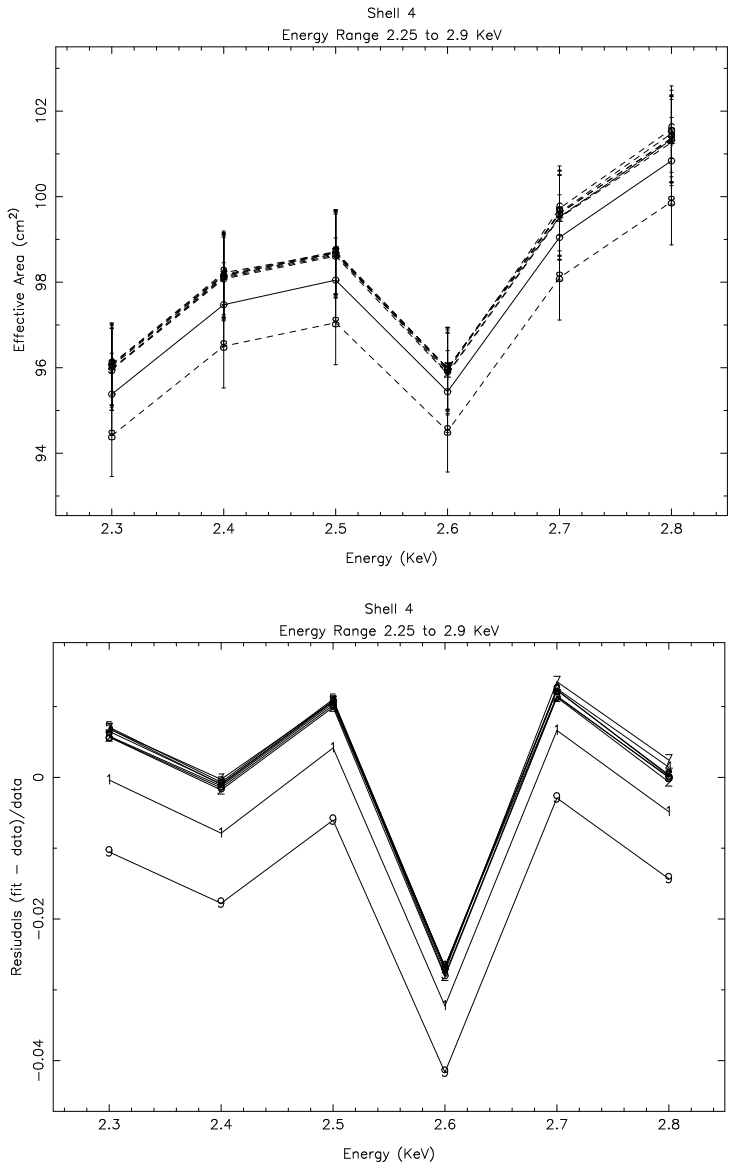

Figure 13.19: SSD continuum data and model effective area and residuals through 2mm pinhole for shell 4 between 2.25 and 2.9 keV.

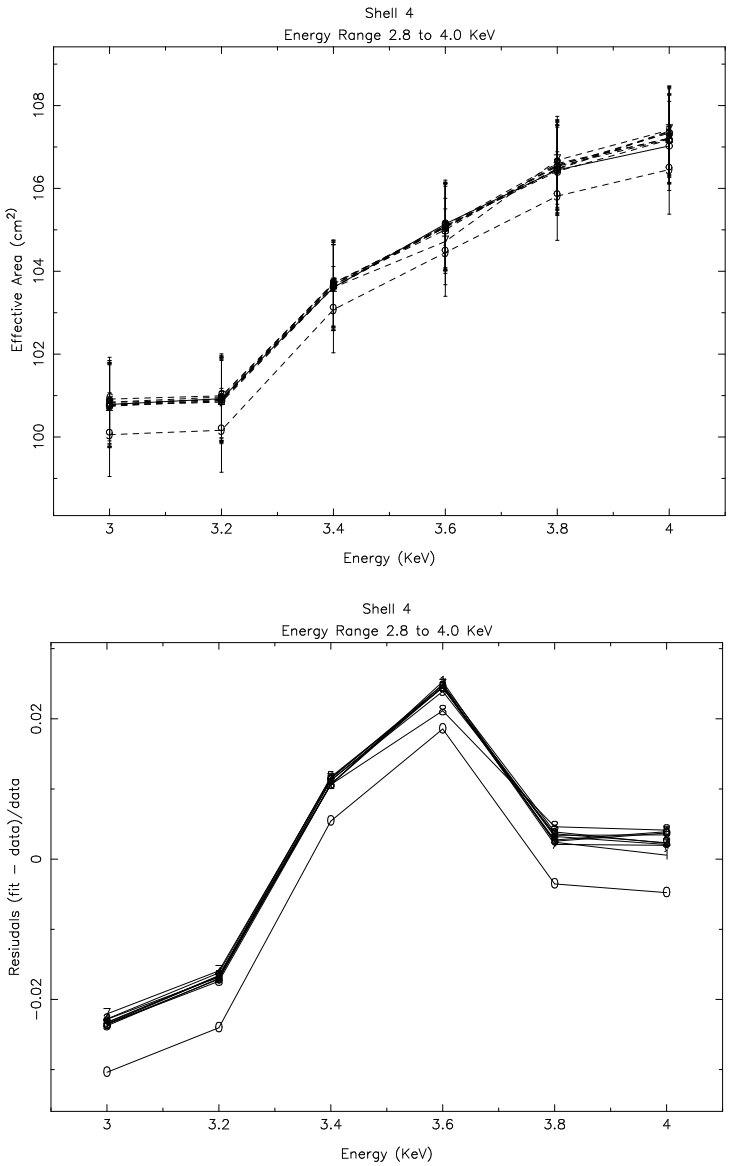

Figure 13.20: SSD continuum data and model effective area and residuals through 2mm pinhole for shell 4 between 2.8 and 4.0 keV.

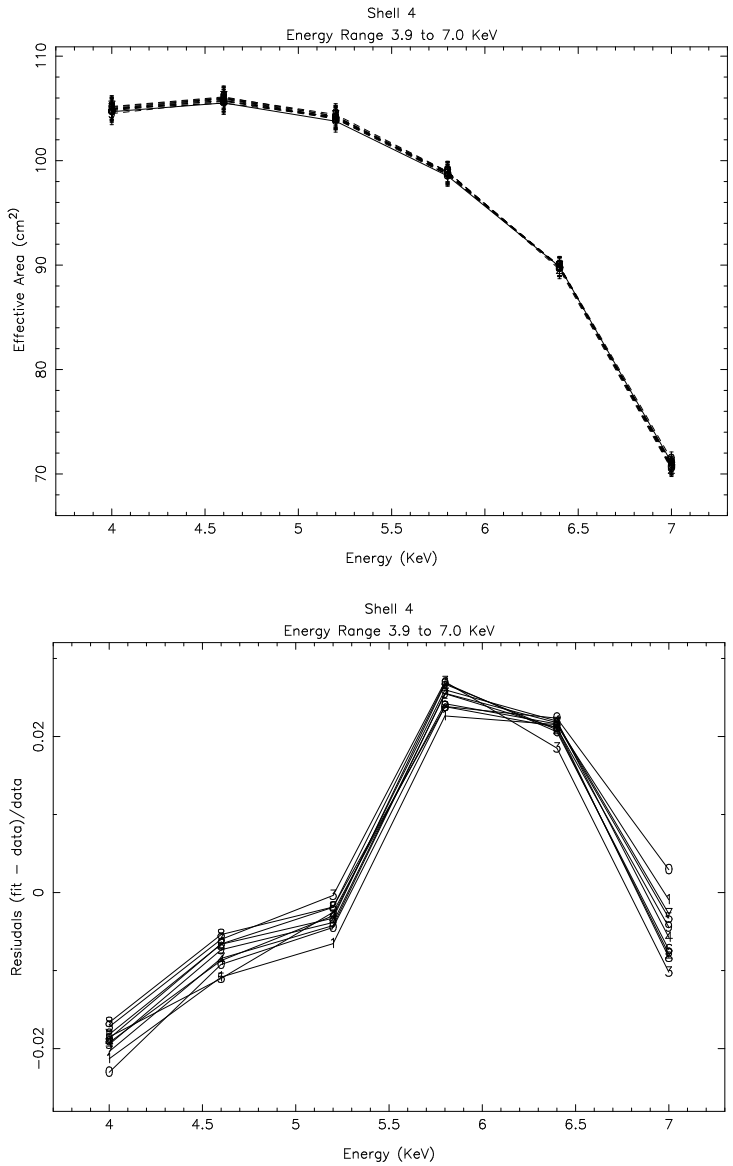

Figure 13.21: SSD continuum data and model effective area and residuals through 2mm pinhole for shell 4 between 3.9 and 7.0 keV.

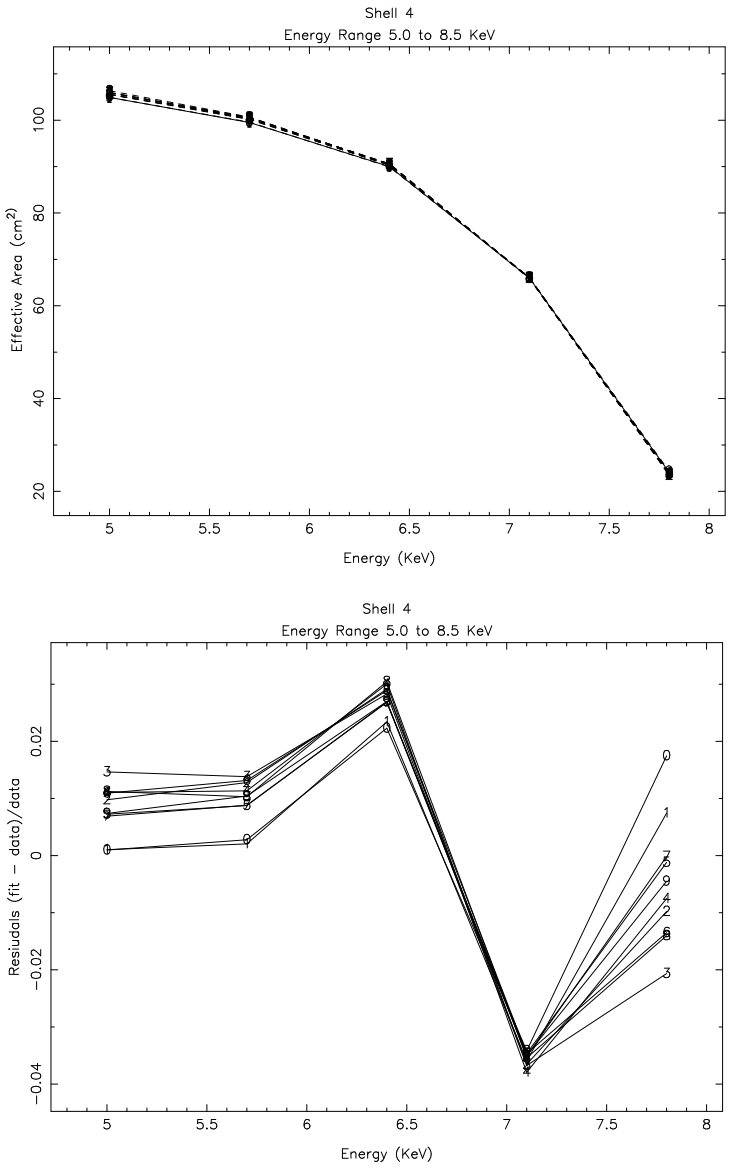

Figure 13.22: SSD continuum data and model effective area and residuals through 2mm pinhole for shell 4 between 5.0 and 8.5 keV.

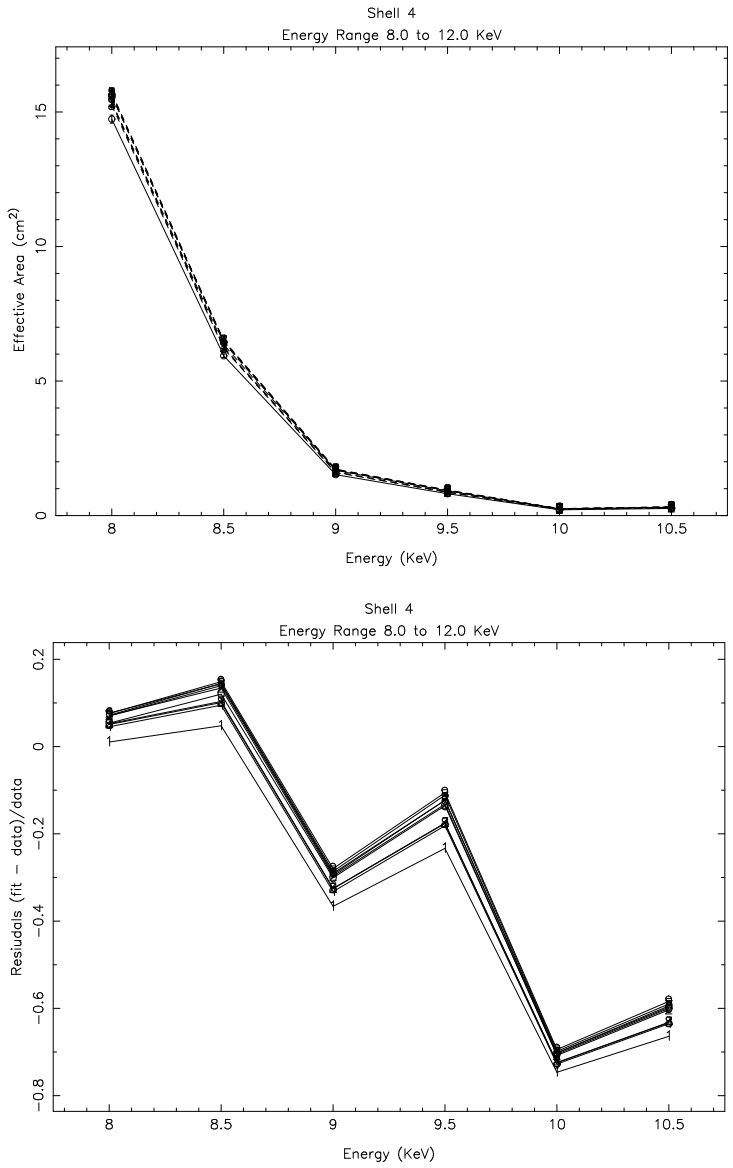

Figure 13.23: SSD continuum data and model effective area and residuals through 2mm pinhole for shell 4 between 8.0 and 12.0 keV.

Since the optical constants used in the model were derived by fitting reflectivity data from witness flats of the mirror, we would expect to get the same values of σ out of the fits to effective area as were used in the fits to reflectivity. Tables 13.2 to 13.5 show the reduced χ^2 of each fit for shells 1, 3, 4, and 6. Also present are the values of σ determined by the fit and the expected value of σ from the synchrotron fits to the reflectivity.

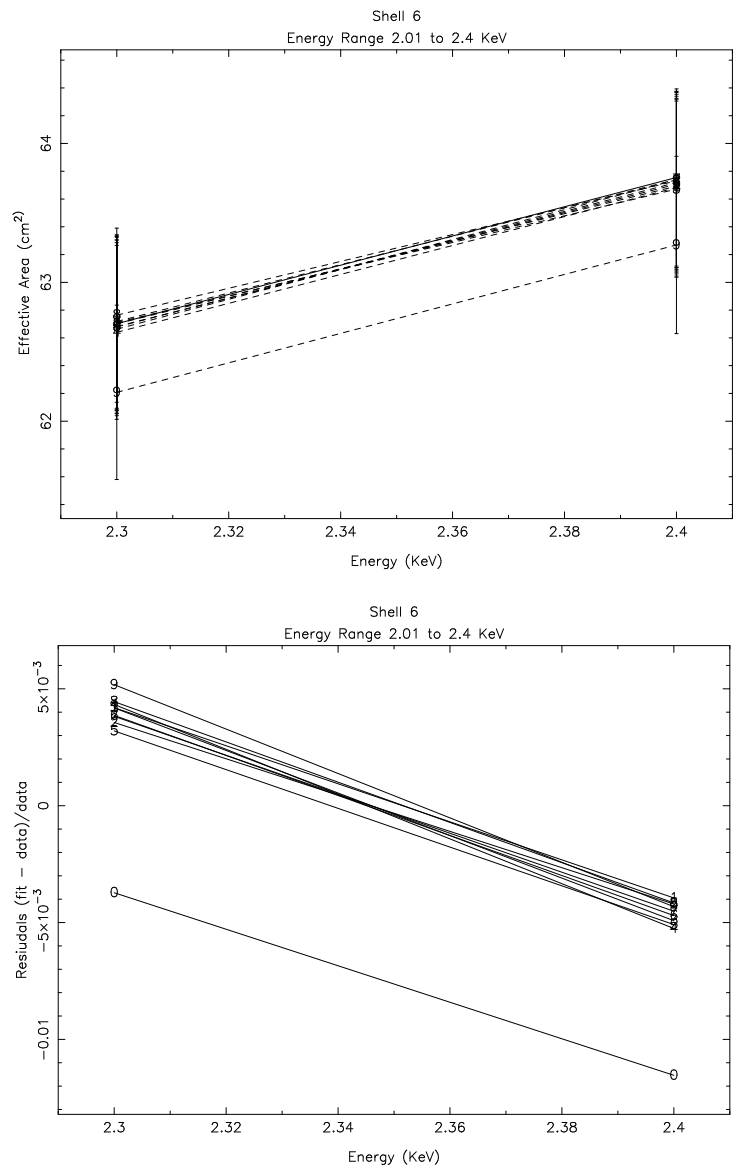

Figure 13.24: SSD continuum data and model effective area and residuals through 2mm pinhole for shell 6 between 2.01 and 2.4 keV.

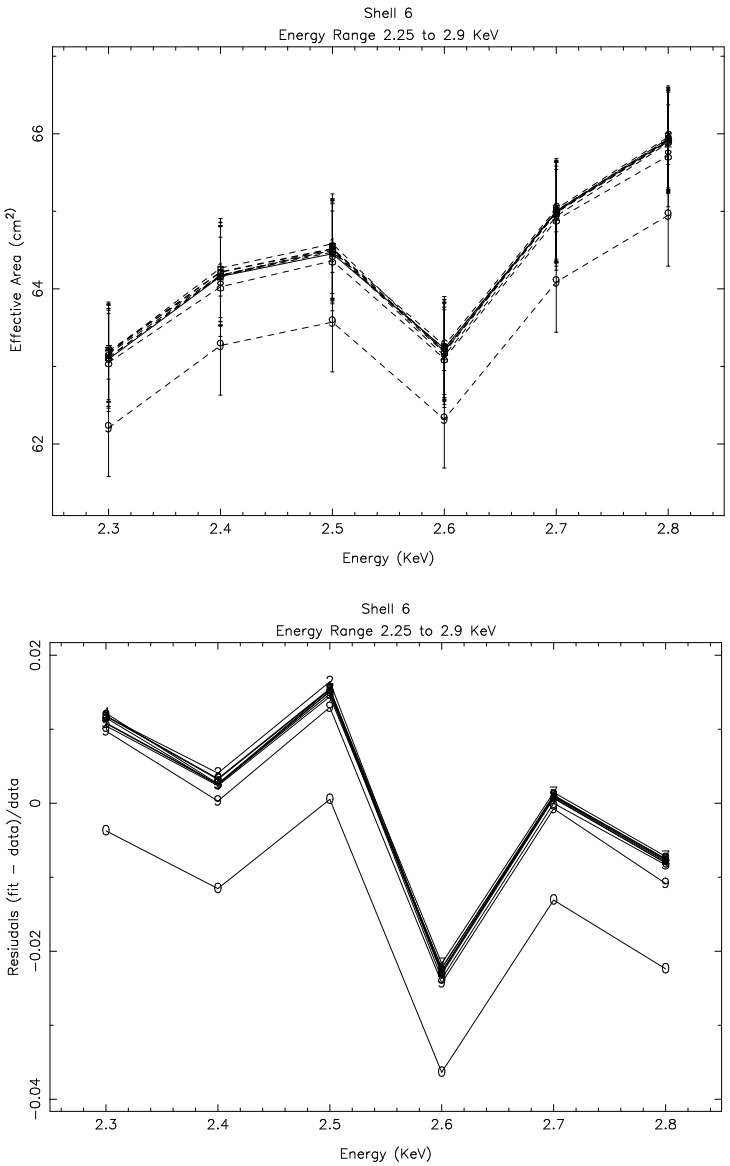

Figure 13.25: SSD continuum data and model effective area and residuals through 2mm pinhole for shell 6 between 2.25 and 2.9 keV.

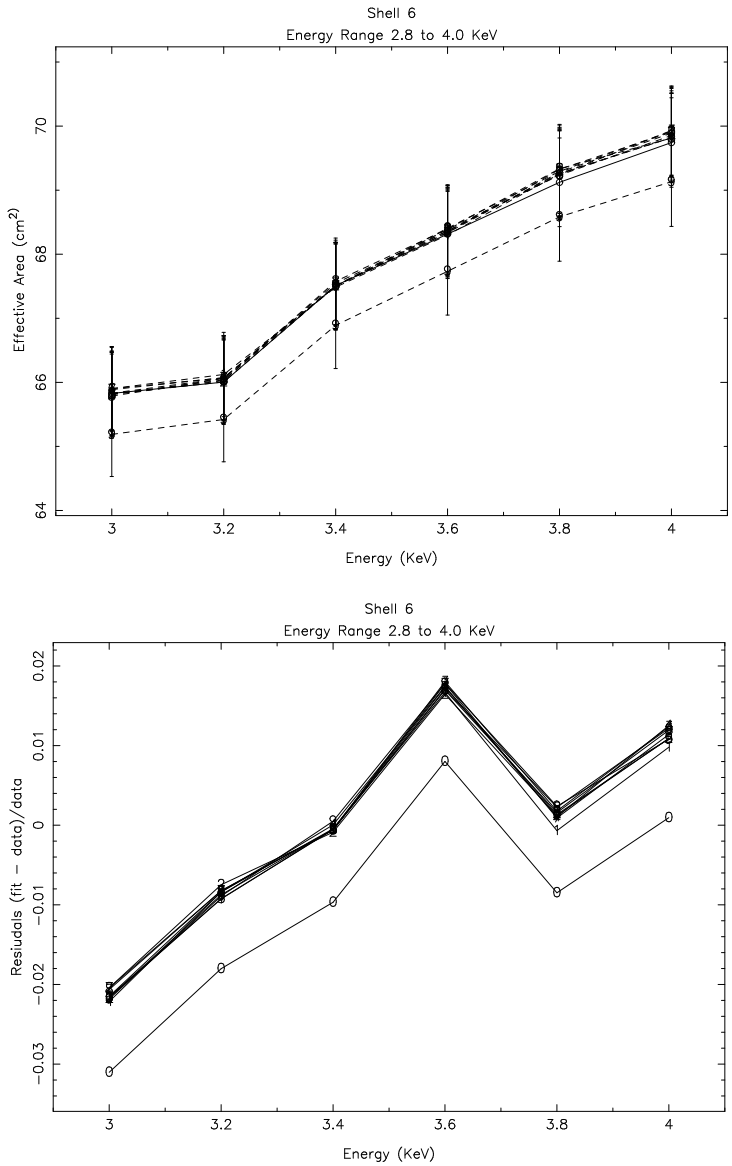

Figure 13.26: SSD continuum data and model effective area and residuals through 2mm pinhole for shell 6 between 2.8 and 4.0 keV.

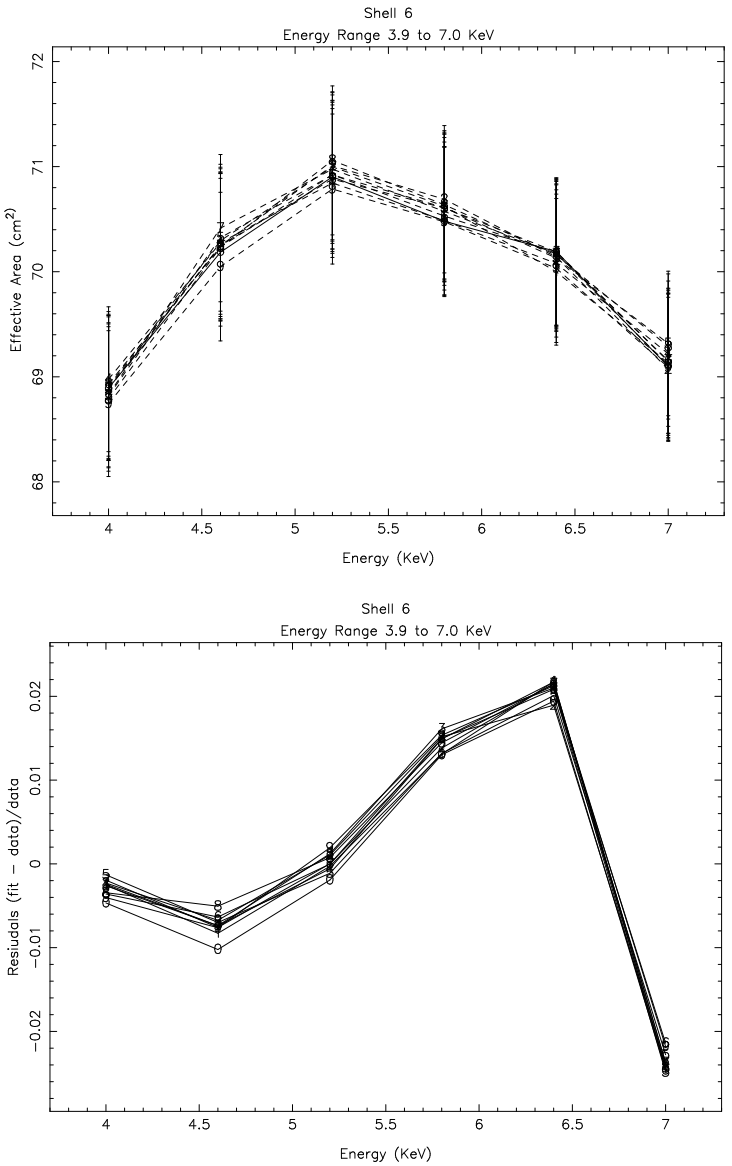

Figure 13.27: SSD continuum data and model effective area and residuals through 2mm pinhole for shell 6 between 3.9 and 7.0 keV.

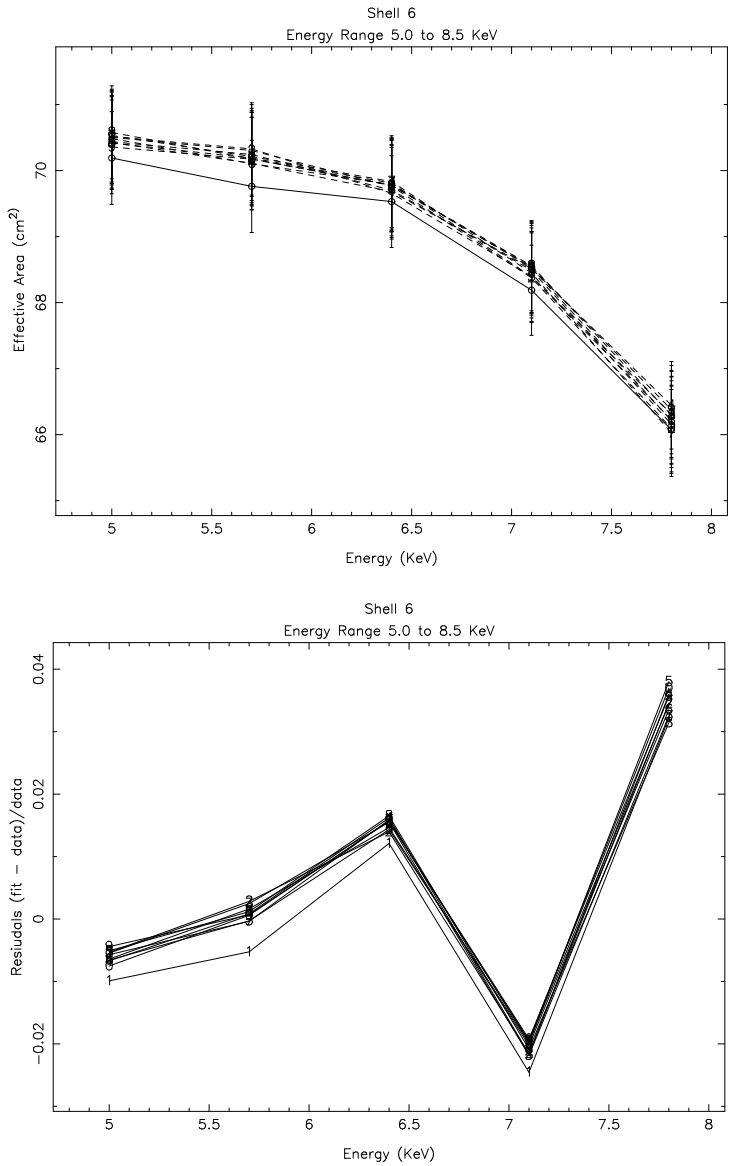

Figure 13.28: SSD continuum data and model effective area and residuals through 2mm pinhole for shell 6 between 5.0 and 8.5 keV.

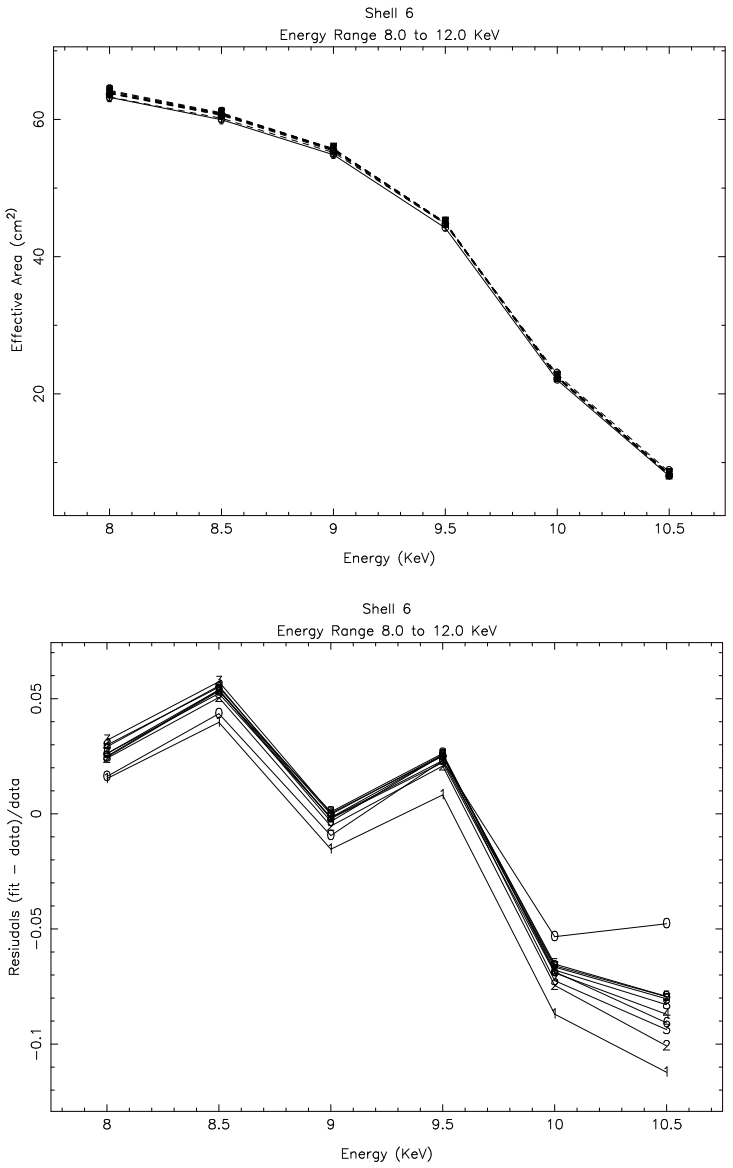

Figure 13.29: SSD continuum data and model effective area and residuals through 2mm pinhole for shell 6 between 8.0 and 12.0 keV.

Energy	Avg Reduced χ^2	$\sigma_{\rm refl}$	Avg $\sigma_{\rm Aeff}$	Avg Residuals
2.01 2.40	0.1278 ± 0.0395	3.9000	7.0903 ± 0.4286	0.8180 ± 0.1099
2.25 2.90	2.3021 ± 0.0737	4.0454	6.8986 ± 0.3962	0.7053 ± 0.0980
2.80 4.00	4.7686 ± 0.2173	3.9000	8.3107 ± 0.2848	1.1310 ± 0.0730
3.90 7.00	19.8605 ± 3.2391	4.2000	8.4641 ± 0.4910	1.0153 ± 0.1169
5.00 8.50	51.0264 ± 4.5356	5.0229	7.7920 ± 0.6637	0.5513 ± 0.1321
8.00 12.00	25.1500 ± 0.5527	4.1000	4.4307 ± 0.2190	0.0807 ± 0.0534

Table 13.2: Shell 1 reduced χ^2 and σ

Energy	Avg Reduced χ^2	$\sigma_{\rm refl}$	Avg $\sigma_{\rm Aeff}$	Avg Residuals
2.01 2.40	0.3366 ± 0.0197	3.9000	6.4552 ± 0.6770	0.6552 ± 0.1736
2.25 2.90	1.7679 ± 0.0841	4.0454	5.6774 ± 0.7523	0.4034 ± 0.1859
2.80 4.00	1.8648 ± 0.0849	3.9000	6.0162 ± 0.6157	0.5426 ± 0.1579
3.90 7.00	4.0426 ± 0.5962	4.2000	6.1872 ± 0.3849	0.4732 ± 0.0916
5.00 8.50	13.2666 ± 2.8037	5.0229	4.7625 ± 0.6406	−0.0518 ± 0.1275
8.00 12.00	41.5906 ± 7.0247	4.1000	3.1486 ± 0.9921	−0.2321 ± 0.2420

Table 13.3: Shell 3 reduced χ^2 and σ

Energy	Avg Reduced χ^2	$\sigma_{\rm refl}$	Avg $\sigma_{\rm Aeff}$	Avg Residuals
2.01 2.40	0.3831 ± 0.7059	3.9000	2.9182 ± 1.3416	−0.2517 ± 0.3440
2.25 2.90	NaN ± NaN	4.0454	NaN ± NaN	NaN ± NaN
2.80 4.00	1.7732 ± 0.1474	3.9000	3.6187 ± 1.1911	−0.0721 ± 0.3054
3.90 7.00	1.1075 ± 0.0877	4.2000	5.6987 ± 0.7249	0.3568 ± 0.1726
5.00 8.50	1.6899 ± 0.2663	5.0229	5.3255 ± 0.5466	0.0602 ± 0.1088
8.00 12.00	18.4686 ± 0.9141	4.1000	4.0980 ± 0.4578	−0.0005 ± 0.1116

Table 13.4: Shell 4 reduced χ^2 and σ

Energy	Avg Reduced χ^2	$\sigma_{\rm refl}$	Avg $\sigma_{\rm Aeff}$	Avg Residuals
2.01 2.40	0.2408 ± 0.1608	3.9000	4.2988 ± 1.6719	0.1022 ± 0.4287
2.25 2.90	1.1571 ± 0.3869	4.0454	3.2510 ± 1.4316	−0.1964 ± 0.3539
2.80 4.00	1.0332 ± 0.1939	3.9000	4.0534 ± 1.2651	0.0393 ± 0.3244
3.90 7.00	0.6554 ± 0.0376	4.2000	5.7636 ± 1.1746	0.3723 ± 0.2797
5.00 8.50	1.1330 ± 0.0711	5.0229	6.4072 ± 1.0825	0.2756 ± 0.2155
8.00 12.00	2.8458 ± 0.4875	4.1000	8.2877 ± 0.3880	1.0214 ± 0.0946

Table 13.5: Shell 6 reduced χ^2 and σ

13.5 Resulting Fits

Figures 13.2to13.5 show the effective areas and residuals from fits to the data over the energy range of 2 to 10.5 KeV. For each shell we see that the quality of the fit deteriorates as the energy increases. For shell 1, the simulated effective areas are within 5% of the data up to 4 KeV, shell 3 is within 5% up to 5 KeV, shell 4 is within 5% up to 7 KeV, and shell 6 is within 5% up to 8 KeV. In each shell, this corresponds with the cut-off energy of the shell where the effective area drops sharply. The data at higher energies, after the cut off, prove difficult to fit as the signal to noise decreases. Thus, the reduced χ^2 of the fits are fairly high, ≈ 20 for shell 1, ≈ 13 for shell 3, ≈ 5 for shell 4, and ≈ 2.5 for shell 6 where the cut off is at a much high energy.

In order to compensate for the difficulty of fitting the entire energy range at once, the data were independently fit over each of the energy ranges used in the synchrotron experiment. Figures 13.6to13.29 illustrate the results of these fits. Notice that the fits get worse for the higher energy ranges, with the effect becoming more pronounced from shell 6 to shell 1. By fitting σ over mulitple energy ranges, the fits improve on the whole. However, despite better fits within the various energy ranges, we do not see the fitted values of σ, σ_{Aeff}, agreeing with the values derived from the synchrotron experiment, σ_{refl}, in Tables 13.2 to 13.5. It should also be noted that thevalues of σ vary from energy range to energy range. While this reflects how σ was handled in deriving the optical constants for the model, it does not reflect the physical nature of σ, a surface grating term. Thus, the quality of the fits have improved to the detriment of the physical model.